ELSEVIER

J. Non-Newtonian Fluid Mech. 116 (2003) 19–32

Journal of Non-Newtonian Fluid Mechanics

www.elsevier.com/locate/jnnfm

Flow instabilities of Herschel–Bulkley fluids

Andreas N. Alexandrou [a,b,*], Philippe Le Menn [b], Georgios Georgiou [c], Vladimir Entov [d]

[a] *Department of Mechanical and Manufacturing Engineering, University of Cyprus, P.O. Box 20537, 1678 Nicosia, Cyprus*
[b] *Semisolid Metal Processing Lab, MPI, Worcester Polytechnic Institute, Worcester, MA 01609, USA*
[c] *Department of Mathematics and Statistics, University of Cyprus, P.O. Box 20537, 1678 Nicosia, Cyprus*
[d] *Institute for Problems in Mechanics, Russian Academy of Science, pr. Vernadskogo, 101, 117526 Moscow, Russia*

Received 25 November 2002; received in revised form 10 January 2003

Abstract

We investigate numerically the interactions of two-dimensional jets of Bingham plastic and Herschel–Bulkley fluids with a vertical surface at a distance from the die exit. This problem simulates the early stages of filling of a planar cavity. Our main objective is to explain the flow instabilities observed during the processing of semisolid materials. The effects of the Reynolds and Bingham numbers and of the inlet boundary conditions on both the filling and the stability of the jet are established by means of numerical time-dependent calculations.

Keywords: Bingham plastic; Herschel–Bulkley model; Cavity filling; Stability; Finite elements

1. Introduction

Recent cavity-filling experiments with semisolid materials, e.g. aluminum slurries, have shown that filling patterns are often irregular and unpredictable, pointing to the existence of flow instabilities which limit the rate of production and affect the final quality of the parts being made. Fig. 1 shows an experimental observation of the so-called “toothpaste” effect which is a typical flow instability observed in semisolid metal processing (SSMP). As the figure shows, even though the two arms are initially symmetric, after the jet hits the closed end of the cavity, the left arm develops a wave-like pattern. The name “toothpaste” comes from the similarity between this instability and the toothpaste behavior when forced out of its tube. A similar jet profile is also shown in Fig. 2. Obviously, such instabilities are undesirable, as they lead to non-uniformities and increase defects such as the porosity in the final parts.

Investigations by Midson et al. [1,2] provide further evidence of these instabilities, and demonstrate experimentally that slow filling yields the ‘best’ die filling behavior, with mostly laminar flow, and the

* Corresponding author.
E-mail address: andalexa@ucy.ac.cy (A.N. Alexandrou).

0377-0257/$ – see front matter © 2003 Elsevier B.V. All rights reserved.
doi:10.1016/S0377-0257(03)00113-7

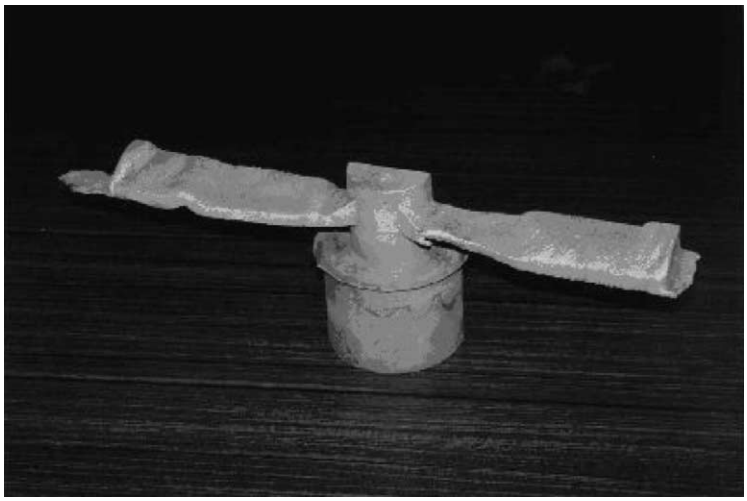

Fig. 1. Flow instability in SSMP: toothpaste behavior. Filling from the center towards the arms (Courtesy of Aluminium Pechiney).

least amount of material folding. In general, the instabilities originate at the point where the filling front in the form of a jet meets the wall of the cavity. Therefore, the jet-vertical wall flow arrangement represents well the early stages of filling of a two-dimensional cavity.

Semisolid slurries are known to exhibit yield stress, τ_o, that is a strong increasing function of the solid fraction, i.e. a decreasing function of the temperature [3]. The most commonly used model to describe fluids with yield is the Bingham model [4,5]:

$$\underline{\dot{\gamma}} = 0 \quad \text{for} \quad \tau \leq \tau_o, \tag{1}$$

$$\underline{\tau} = \left(\eta + \frac{\tau_o}{\dot{\gamma}}\right)\underline{\dot{\gamma}} \quad \text{for} \quad \tau > \tau_o, \tag{2}$$

where $\underline{\tau}$ is the viscous stress tensor, $\underline{\dot{\gamma}}$ the rate of deformation tensor, defined as

$$\underline{\dot{\gamma}} = \tfrac{1}{2}[\nabla \boldsymbol{u} + (\nabla \boldsymbol{u})^{\mathrm{T}}], \tag{3}$$

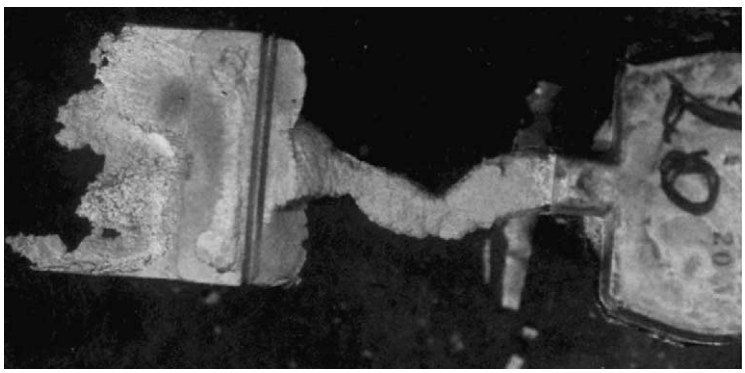

Fig. 2. Flow instability in SSMP: toothpaste behavior. Filling from the right to the left (Courtesy of Aluminium Pechiney).

$\boldsymbol{u}$ is the velocity vector, and T denotes the transpose of the velocity gradient tensor, $\nabla\boldsymbol{u}$. In Eqs. (1) and (2), τ and $\dot{\gamma}$ are, respectively, the second invariants of the stress and rate of strain tensors, and η is the viscosity of the deformed material. The rheological behavior of a Bingham fluid is characterized by two different flow regimes: if $\tau \leq \tau_o$, the material behaves as a rigid solid, whereas, if $\tau \geq \tau_o$, it flows with apparent viscosity $\eta_{app} = \eta + (\tau_o/\dot{\gamma})$. The two distinct fluid regions, yielded ($\tau > \tau_o$) and unyielded ($\tau < \tau_o$), are separated by the "yield surface" defined as the surface where $\tau = \tau_o$.

The Herschel–Bulkley model is a generalization of the Bingham model that takes into account changes in the effective viscosity with the applied shear rate through a power-law behavior:

$$\eta = \kappa\dot{\gamma}^{n-1}, \tag{4}$$

where n and κ are, respectively, the power-law exponent and the consistency index.

In numerical modeling, in addition to the non-linearities in the governing equations, an inherent difficulty of the Bingham and Herschel–Bulkley models is that they are discontinuous. Due to the presence of $\dot{\gamma}$ in the denominator of Eq. (2), at vanishing shear rates, the apparent viscosity becomes unbounded. Also, while calculating the velocity field, the shape and location of the yield surface are unknown. This introduces significant difficulties in the simulations of complicated problems that are only amenable to numerical analysis. To overcome these issues, several modified versions of Eqs. (1) and (2) have been proposed that approximate the rheological behavior of the fluid to be valid uniformly at all levels of stress [6–9]. Papanastasiou [6] introduced a regularization parameter m that controls the exponential rise in the stress at low rates of strain:

$$\underline{\underline{\tau}} = \left[\eta + \tau_o \frac{1 - \exp(-m\dot{\gamma})}{\dot{\gamma}}\right]\underline{\underline{\dot{\gamma}}}. \tag{5}$$

The parameter m has dimensions of time. The Papanastasiou model can be generalized to the Herschel–Bulkley fluid by specifying $\eta = \kappa\dot{\gamma}^{n-1}$. The Bingham-plastic behavior is approximated for relatively large values of m. According to Eq. (5), for $\dot{\gamma} \approx 0$, the apparent viscosity is finite, given by $\eta_{app} \approx (\eta + m\tau_o)$. Papanastasiou validated this model on several simple flows, such as one-dimensional channel flow, two-dimensional boundary layer flow, and extrusion flow [6]. The accuracy and effectiveness of generalized models, such as the one described by Eq. (5), in representing fluids with yield stress has been demonstrated for various flows by Ellwood et al. [10], Mitsoulis et al. [11], Tsamopoulos et al. [12], Blackery and Mitsoulis [13], Beaulne and Mitsoulis [14], Burgos and coworkers [9,15], Smyrnaios and Tsamopoulos [16], and Alexandrou et al. [17].

The use of regularized models can be supported by experimental data reported by Ellwood et al. [10], Keentok et al. [18] and Dzuy and Boger [19], which demonstrate that, in certain cases, a continuous model provides a better approximation to experimental data than the ideal model. Therefore, it is postulated that the ideal Bingham model may be only a theoretical idealization.

In a recent study, Alexandrou et al. [20] investigated the filling of a planar cavity with Bingham fluids by means of time-dependent, finite-volume calculations using the Papanastasiou model. They examined the relative importance of inertial, viscous and yield stress effects on the filling profiles. They identified five characteristic filling patterns: "mound," "disk," "shell," "bubble" and a "transition" between that of "mound" and "bubble" patterns. A summary of these different flow behaviors is shown in Fig. 3, in which the flows are from the right to the left. These characteristic flow patterns highlight the important role of the finite yield stress in Bingham fluids. Experimental studies confirmed the existence of the numerically obtained patterns; the "mound," "disk," and "shell" patterns have been observed by Paradies

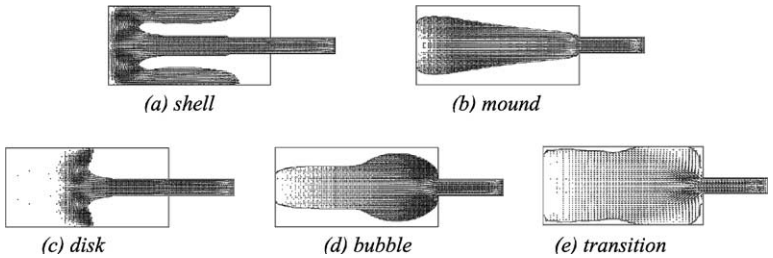

Fig. 3. Summary of the flow patterns observed in 2-D die filling [20]. All flows are from the right to the left. (a) $Re = 50$, $Bi = 0$; (b) $Re = 0.05$, $Bi = 0.2$; (c) $Re = 50$, $Bi = 10$; (d) $Re = 50$, $Bi = 200$; (e) $Re = 12$, $Bi = 9.4$.

and Rappaz [21] in semisolid processing. Recent experimental results by Koke et al. [22] also confirmed these patterns by using model substances such as chocolate cream, calcium-carbonate/oil suspension, tomato paste, ultrasonic gel and Newtonian silicone oil.

The main objective of the present work is to investigate by means of time-dependent finite-element calculations the stability of jets of Bingham-plastic and Herschel–Bulkley fluids emanating from a die and impinging on a vertical wall. As discussed above, this flow arrangement simulates also the early stages of filling of a two-dimensional cavity. These flows are in reality the stable configurations of the flows examined by Alexandrou et al. [20]. Since their results were obtained using a finite volume method, for validation purposes, we also simulated the cases considered in [20]. In Section 2, the governing equations and the boundary and initial conditions are presented. In Section 3, the numerical method is briefly discussed. In Section 4, the numerical results are presented and discussed. Finally, in Section 5, we provide a summary of the results and draw conclusions.

2. Governing equations and numerical method

The schematic of the flow problem is shown in Fig. 4. The 2-D geometry is characterized by the inlet section (length l and height H). The material is injected in the die from the left side and hits the vertical

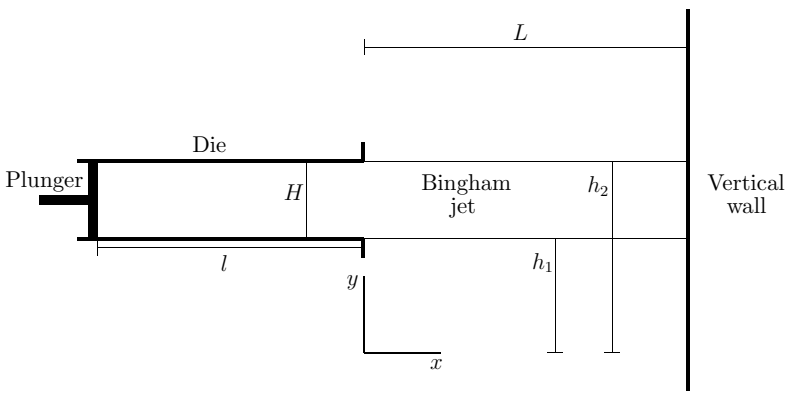

Fig. 4. Geometry of the two-dimensional cavity and initial position of the jet.

solid surface at a distance L away. The flow is modeled using the conservation of mass and momentum for an incompressible fluid:

$$\nabla \cdot \boldsymbol{u} = 0, \tag{6}$$

$$\rho \left[\frac{\partial \boldsymbol{u}}{\partial t} + \boldsymbol{u} \cdot \nabla \boldsymbol{u} \right] = \nabla \cdot \underline{\sigma}, \tag{7}$$

where ρ is the density of the fluid, and $\underline{\sigma}$ the total stress tensor, given by

$$\underline{\sigma} = -p\,\underline{I} + \underline{\tau}.$$

Here, p represents the total pressure and $\underline{I}$ the unit tensor. The body force per unit volume due to gravity has been neglected.

The set of governing equations (Eqs. (6) and (7)) are non-dimensionalized using the following scales:

$$x_i^* = \frac{x_i}{H}, \quad t^* = \frac{t}{H/U_\mathrm{o}}, \quad \boldsymbol{u^*} = \frac{\boldsymbol{u}}{U_\mathrm{o}}, \quad p^* = \frac{p}{\tau_\mathrm{o}}, \quad \underline{\tau}^* = \frac{1}{\tau_\mathrm{o}}\underline{\tau}, \quad \underline{\sigma}^* = \frac{1}{\tau_\mathrm{o}}\underline{\sigma}, \tag{8}$$

where the asterisks denote the non-dimensional variables, and U_o is the average inlet velocity. With the above scalings, the imposed volumetric flow rate is equal to unity. The non-dimensionalized governing equations become:

$$\nabla \cdot \boldsymbol{u}^* = 0, \tag{9}$$

and

$$Re \left[\frac{\partial \boldsymbol{u}^*}{\partial t^*} + \boldsymbol{u}^* \cdot \nabla \boldsymbol{u}^* \right] = Bi\, \nabla \cdot \underline{\sigma}^*, \tag{10}$$

where *Re* and *Bi* are the Reynolds and Bingham numbers, respectively, defined by

$$Re = \frac{\rho U_\mathrm{o}^{(2-n)} H^n}{\kappa} \quad \text{and} \quad Bi = \frac{\tau_\mathrm{o} H^n}{\kappa U_\mathrm{o}^n}, \tag{11}$$

in the case of a Herschel–Bulkley fluid, and by

$$Re = \frac{\rho U_\mathrm{o} H}{\eta} \quad \text{and} \quad Bi = \frac{\tau_\mathrm{o} H}{\eta U_\mathrm{o}} \tag{12}$$

in the case of a Bingham fluid.

The dimensionless form of the regularized Herschel–Bulkley constitutive relation is:

$$\underline{\tau}^* = \left[\frac{1}{Bi} \dot{\gamma}^{*(n-1)} + \frac{[1 - \exp(-m^* \dot{\gamma}^*)]}{\dot{\gamma}^*} \right] \underline{\dot{\gamma}}^*, \tag{13}$$

where $\underline{\dot{\gamma}}^*$ is the dimensionless rate of strain tensor, $\dot{\gamma}^*$ denotes its second invariant, and m^* the dimensionless growth exponent:

$$\underline{\dot{\gamma}}^* = \frac{1}{U_\mathrm{o}/H}\underline{\dot{\gamma}}, \quad \dot{\gamma}^* = \frac{\dot{\gamma}}{(U_\mathrm{o}/H)^2}, \quad m^* = \frac{m U_\mathrm{o}}{H}. \tag{14}$$

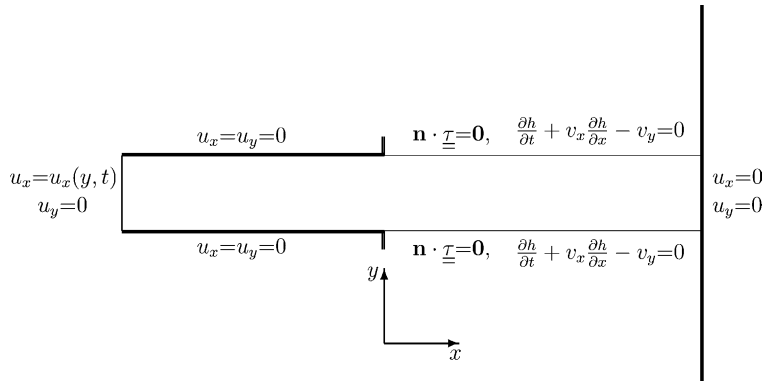

Fig. 5. Boundary conditions.

2.1. Boundary and initial conditions

The boundary conditions for the flow problem studied here are shown in Fig. 5. Along the two walls of the die and the vertical wall, the velocity is set to zero (no slip). Along the two free surfaces, surface tension is neglected, and thus the normal and tangential stress components vanish:

$$\boldsymbol{n}\cdot\underline{\underline{\tau}}=0, \tag{15}$$

where $\boldsymbol{n}$ is the outward unit normal vector to a free surface. Another condition at the two free surfaces is the kinematic one,

$$\frac{\partial h}{\partial t}+u_x\frac{\partial h}{\partial x}-v_y=0, \tag{16}$$

which provides the additional equation required for the calculation of the unknown positions of the two free surfaces, $h_1(x,t)$ and $h_2(x,t)$.

At the entrance plane, taken at a distance l from the die exit, the y-velocity component is set to zero. In all the runs the x-velocity is assumed to be (at all times) the parabolic solution corresponding to the fully-developed channel flow of a Newtonian fluid, such that the dimensionless volumetric flow rate $Q=1$. As explained below, for the unsteady cases the symmetry of the velocity profile is altered initially for a short time Δt in order to simulate the instabilities. Note also that since the velocity distribution of fully developed channel flow of Herschel–Bulkley fluids is not exactly parabolic, the inlet length is fixed at a distance l from the die exit in order to allow the profile to develop fully prior to reaching the exit. The selected length $l=5$, is found to be sufficiently long to ensure that the flow prior to the exit is indeed fully developed. As discussed later in Section 4, in order to simulate the toothpaste effect, a brief artificial disturbance is introduced to disrupt the symmetry of the flow leading to an asymmetric, piecewise-parabolic profile.

The initial condition corresponds to the steady-state solution of the same flow in the case of flat free surface and in the absence of the vertical wall, i.e. the solution of the die-swell flow problem. The time-dependent calculations are initiated by introducing the vertical wall by setting the exit velocity to zero, Fig. 5.

3. Finite element formulation

The continuity and momentum equations are discretized in space, using the classical mixed-Galerkin finite element method with nine-velocity-node and four-pressure-node quadrilateral elements, and integrated in time using fully-implicit finite differences. The unknown positions of the two free surfaces are calculated simultaneously with the velocity and pressure fields. Quadratic basis functions are introduced, in order to expand the unknown positions, h_1 and h_2, of the two free surfaces and to weight the kinematic condition. At each time step, the resulting non-linear discretized system of equations is solved using the Newton–Raphson method. At each Newton iteration, the finite-element mesh is automatically restructured according to the new positions of the two free surfaces using the spine technique while the number of elements is kept the same. More details about the numerical method are given in refs. [23,24].

4. Numerical results

As stated earlier, in this work, we concentrate on a problem equivalent to that of the early stages of die filling, i.e. the interaction of a Herschel–Bulkley fluid jet and a vertical surface at a distance L from the die exit and we study the interplay between inertia, viscous drag and yield stress, or as expressed in terms of force per unit depth, $F_i \equiv \rho U_o^2 H$, $F_v \equiv \eta U_o$, and $F_{\tau_o} \equiv \tau_o H$, respectively. The Reynolds number represents the F_i/F_v ratio, while the Bingham number indicates the F_{τ_o}/F_v ratio. The effects of *Re* and *Bi* are investigated using the two-dimensional geometry shown in Fig. 4.

The parameter m in the regularized model is set to a value of $m = 1000$, which is found to be sufficiently high to insure converged results with respect to m. A more pertinent study of the effect of m on the accuracy of the results can be found in [9,15]. The reported results are also mesh and time-step independent. A typical finite element mesh used in the simulations is shown in Fig. 6. This is refined around flow singularities and in regions where gradients are large (i.e. around the die exit and the end-wall).

Fig. 7 shows results for $n = 1$ (Bingham plastic) and conditions similar to those in [20]. The five typical flow behaviors reported in [20] and shown in Fig. 3, i.e. the “shell”, “disk”, “mound”, “bubble” and “transition” patterns, have been reproduced here as well, providing thus further supporting evidence on their existence. Note that case (a) corresponds to the early stages when the jet hits the wall. Further, simulation of this flow is not possible with the present code. It should be noted that, unlike Fig. 3, the flows are from the left to the right. The corresponding flow parameters for these typical patterns are tabulated

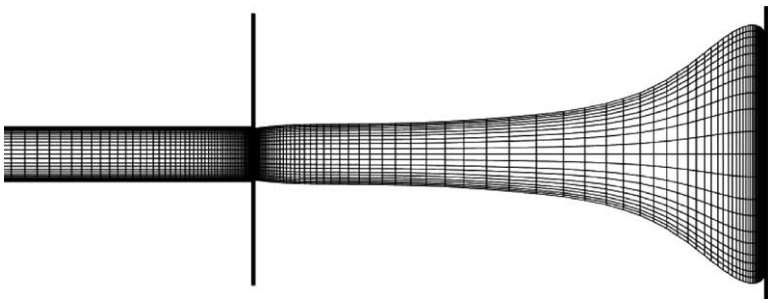

Fig. 6. Geometry and finite element mesh.

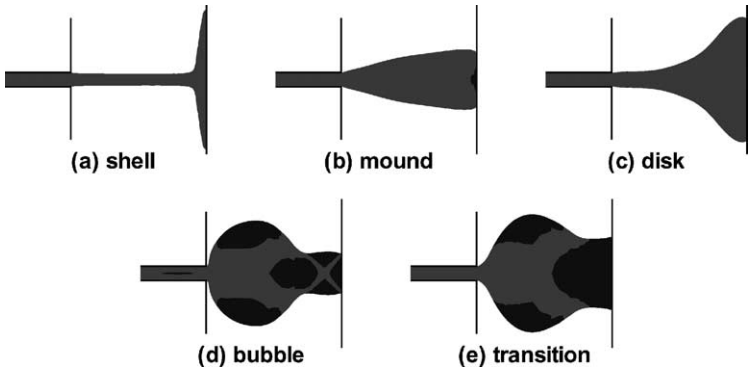

Fig. 7. Summary of the flow patterns observed for the $L = 10$ geometry. Yielded (light-color) and unyielded (dark-color) regions are highlighted. The flows are from the left to the right.

in Table 1. Fig. 7 also shows the topography of the yielded and unyielded regions. We observe that only the "bubble" and "transition" patterns exhibit significant unyielded zones. Therefore, the first three patterns correspond to the behavior of a viscous fluid. The "bubble" and "transition" patterns, though, are expected to be influenced by the yield stress effects. As it will be demonstrated below, flow instabilities are primarily connected to these two patterns.

Note here that numerical simulations of flows that in real life are unstable may fail to predict flow instabilities, due to the almost perfect symmetry of numerical results, and due to the fact that numerical errors take a long time to grow to a magnitude that can trigger instabilities. Therefore, it is customary to introduce an artificial disturbance to disrupt the symmetry of the flow. This artificial instability is typically very small, and it is applied for a short duration. Here, a disturbance is introduced in the flow by imposing at the inlet the asymmetric velocity profile of Fig. 8 for a short time Δt. For $t \geq \Delta t$, the inlet velocity is kept constant and symmetric. In both the symmetric and asymmetric cases, the volumetric flow rate is kept constant at all times. The flow field and the jet stability are found to be independent of the magnitude and the duration of the asymmetry.

Typical jet-wall interactions obtained numerically for $L = 10$ are shown in Figs. 9 and 10, as sequences of 'snapshots' of the jet profile, where t is the non-dimensional time. In both cases, the inlet velocity profile is disturbed from $t = 0$ until $t = \Delta t = 1.5$. Fig. 9 shows the jet behavior at a low Reynolds number ($Re = 1$) and at a moderate Bingham number ($Bi = 3$). For an undisturbed, symmetric velocity profile at the inlet, these conditions lead to a "bubble" pattern. In the case of the disturbed velocity

Table 1
Parameters used for the flow patterns in Fig. 7 ($L = 10$)

Re	*Bi*	Flow Pattern
500	10	Shell
6	0.1	Disk
0.5	0.1	Mound
1	3	Bubble
10	1.7	Transition

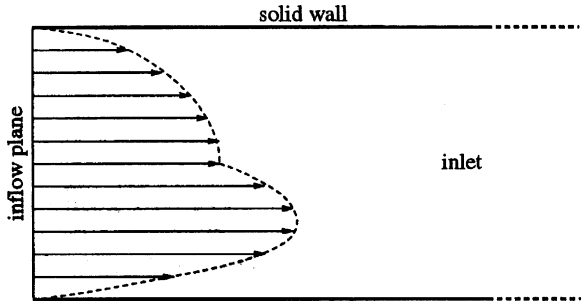

Fig. 8. The shape of the perturbed inlet velocity profile that is introduced for a short duration, $0 \leq t \leq \Delta t$.

profile, the emanating jet grows as a "bubble" up to a dimensionless time $t \approx 7$. After this time, the disturbance triggers an instability which forces the jet to bend, very much like the buckling of a slender solid column. This flow behavior is very similar to what it is observed experimentally and is described as the "toothpaste" effect. For the discussion that follows such behavior is labeled as "unstable".

The flow shown in Fig. 10 is obtained for $Re = 5$ and $Bi = 1$. For both symmetric and asymmetric flow conditions the jet grows in a manner consistent with a "transition" pattern. Therefore, the initial disturbance has no impact on the stability of the jet, and no noticeable difference can be observed between the symmetric and asymmetric cases. In the discussion below this flow behavior is labeled as "stable."

Fig. 11 shows a complete map of the jet profiles as a function of the Reynolds and Bingham numbers for the range $0.5 \leq Re \leq 50$, $0 < Bi \leq 40$. This map clearly shows the regions where "stable" and

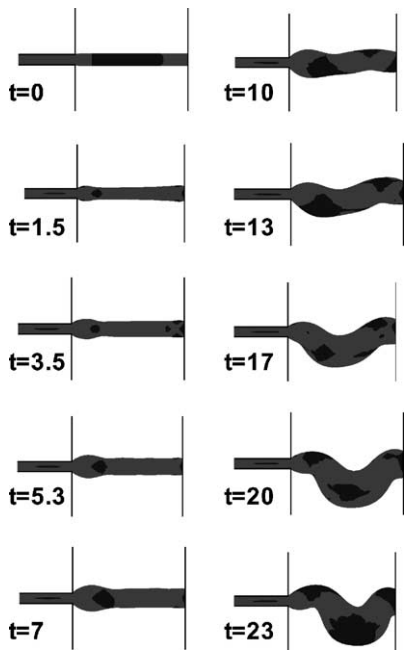

Fig. 9. Toothpaste behavior, $Re = 1$, $Bi = 3$, $L = 10$. The disturbance is imposed from $t = 0$ until $t = 1.5$.

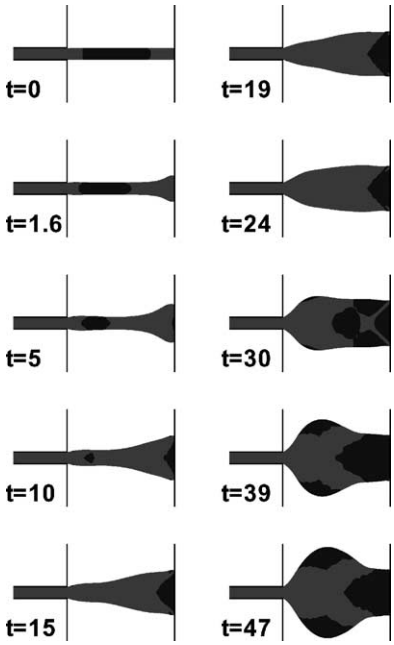

Fig. 10. Stable jet behavior, $Re = 5$, $Bi = 1$, $L = 10$. The disturbance is imposed from $t = 0$ until $t = 1.5$.

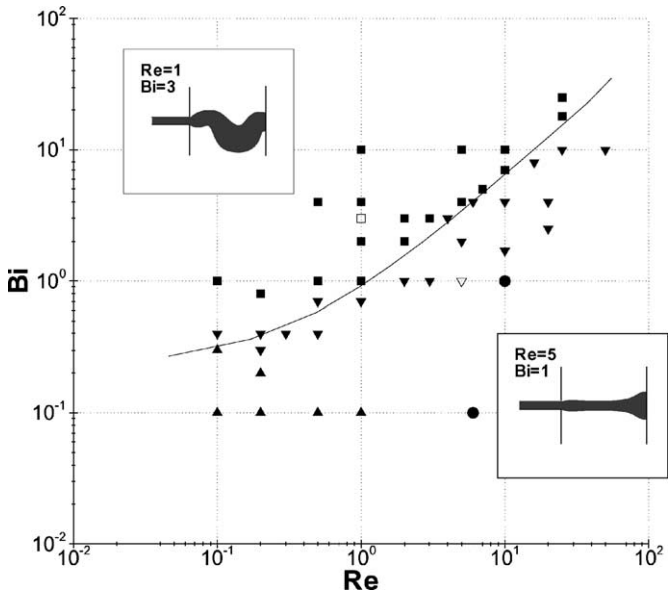

Fig. 11. Stability of the jet when hitting a vertical surface ($L = 10$), the Reynolds and Bingham numbers being the control parameters. (▲) "mound" pattern; (●) "disk" pattern; (■) "bubble" pattern; (▼) "transition" pattern. The hollow symbols (□ and ▽) represent the cases discussed in detail and pictured on the map. The estimated boundary between the stable and unstable behaviors has been sketched in. Stable and unstable behaviors are, respectively, below and above this limiting line.

"unstable" patterns occur. The estimated boundary between these two zones is sketched in order to demarcate the range of *Re* and *Bi* which they correspond to. On this map, the symbols ▲, ●, ■ and ▼ represent, respectively, the "mound," "disk," "bubble" and "transition" patterns. The hollow symbols (□ and ▽) represent the cases discussed in detail (Figs. 9 and 10). As speculated, while the "bubble" pattern leads to unstable jet behavior, "shell," "disk" and "mound" patterns are stable and most of the "transition" cases lead to stable jet profiles. The "bubble" pattern is very sensitive to flow instabilities, that prevent this pattern to develop. These numerical results explain why experimental observations of the "bubble" pattern are not as common as the other patterns. It is concluded from the results that the instabilities are the result of the finite yield stress and the way yielded and unyielded regions interact with each other.

The effect of the distance between the die exit and the vertical wall is established by using three different lengths $L = 10$, 15 and 20. Fig. 12 highlights this effect on the stability of the jet for $Re = 1$ and $Bi = 0.7$. The jet behavior is either stable and symmetric ($L = 10$) or unstable and toothpaste-like ($L = 15$ and 20). This demonstrates that the longer the distance of the wall from the slit exit, the more likely it is to observe the toothpaste instability. Fig. 13 summarizes this behavior for the three lengths used. The map shows the estimated boundaries between stable and unstable jet behavior.

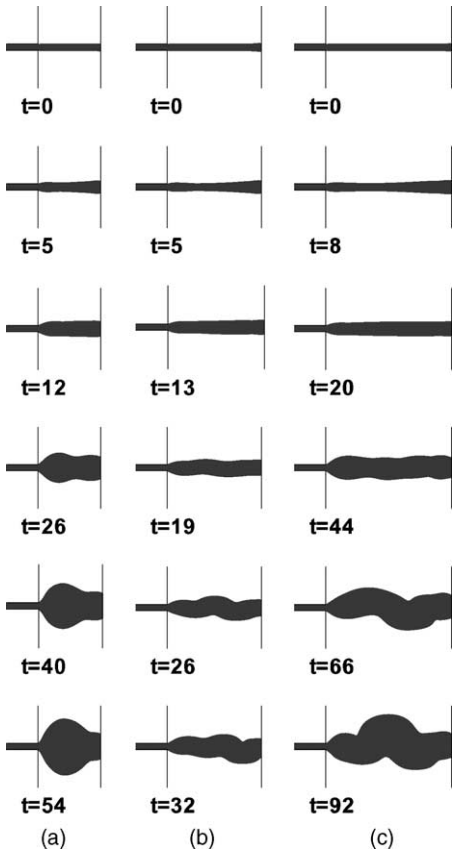

Fig. 12. Stability of the flow ($Re = 1$, $Bi = 0.7$) for three different jet lengths: (a) $L = 10$; (b) $L = 15$; (c) $L = 20$.

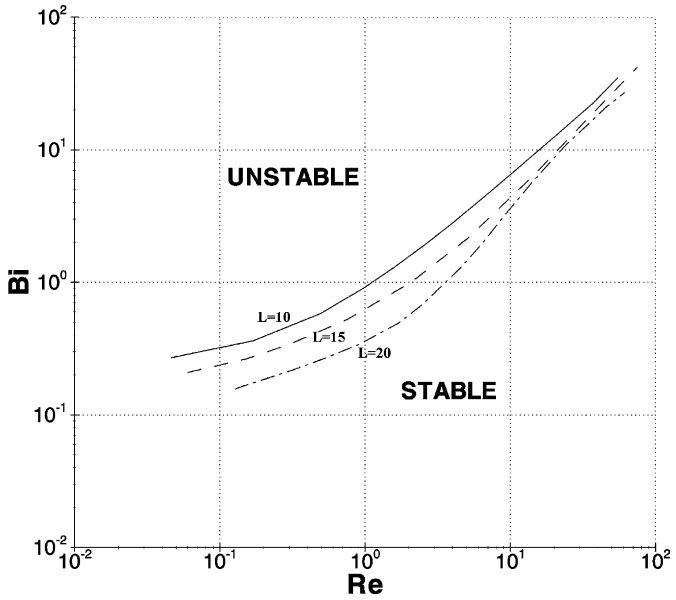

Fig. 13. Estimated stability limits for different jet lengths: $L = 10$ (solid line), $L = 15$ (dashed line) and $L = 20$ (dash-dotted line).

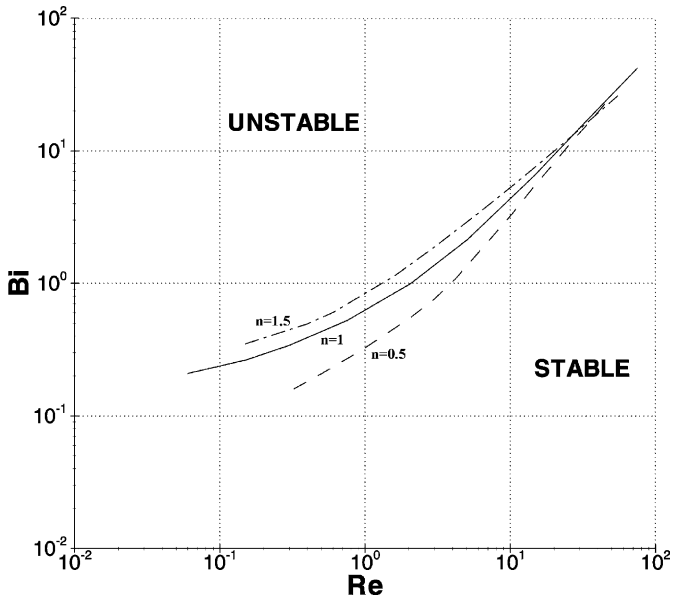

Fig. 14. Estimated stability limits for different power-law coefficients: $n = 1$ (solid line), $n = 0.5$ (dashed line) and $n = 1.5$ (dash-dotted line).

The results shown so far are for Bingham fluids ($n = 1$). The effect of the power-law exponent is studied by considering two new cases: one corresponding to a shear-thinning fluid ($n = 0.5$) and another to a shear-thickening fluid ($n = 1.5$). For both cases, the distance of the wall from the exit is set to $L = 15$. Fig. 14 shows the corresponding stability diagrams. Again, limiting lines separate stable and unstable behaviors. A shift between the three limiting lines can be observed: the smaller the power-law index, the more unstable the flow is. In other words, a shear-thinning behavior is more sensitive to instabilities than a shear-thickening one. It appears also that the power-law index becomes less important (actually it is not important at all) for large values of *Bi*. This is due to the fact that for large *Bi* the flow behaves more like a solid as very little of the fluid deforms.

5. Conclusions

The numerical simulations presented in this study verify the importance of the finite yield stress in Herschel–Bulkley flows. The results confirm the existence of five characteristic flow patterns ("shell," "disk," "mound," "bubble" and "transition") that have been observed both experimentally and numerically. By controlling flow parameters, one may be able to a priori fix the jet behavior which leads to desirable quality and properties of the final parts.

In actual Herschel–Bulkley flows, the injection process is very sensitive to flow instabilities which may lead to irregular and unpredictable filling patterns. This undesired behavior is likely to happen at distinct combinations of flow parameters. Stability maps of the injection process have been drawn as a function of these parameters. It is concluded that the most unstable pattern is that of "bubble" and to a lesser degree that of the "transition" pattern, primarily due to the effects of the yield stress.

Acknowledgements

Partial support for this study was provided by Aluminium Pechiney, France.

References

[1] S.P. Midson, R.B. Minkler, H.B. Brucher, Gating of semisolid aluminum castings, in: Proceedings of the 6th International Conference on Semisolid Processing of Alloys and Composites, Turin, 27–29 September 2000, p. 67.
[2] S.P. Midson, L.E. Thornhill, K.P. Young, Influence of key process parameters on the quality of semisolid metal cast aluminum components, in: Proceedings of the 5th International Conference on Semisolid Processing of Alloys and Composites, Golden, Colorado, 23–25 June 1998, p. 181.
[3] A. Ahmed, A.N. Alexandrou, Processing of semisolid materials using a shear-thickening Bingham fluid model, in: Proceedings of the 1994 ASME Fluids Engineering Division Summer Meeting, FED-vol. 179, New York, 1994, p. 83.
[4] E.C. Bingham, Fluidity and Plasticity, McGraw-Hill, New York, 1922.
[5] R.B. Bird, G.C. Dai, B.J. Yarusso, The rheology and flow of viscoplastic materials, Rev. Chem. Eng. 1 (1983) 1.
[6] T.C. Papanastasiou, Flows of materials with yield, J. Rheol. 31 (1987) 385.
[7] M. Bercovier, M. Engelman, A finite element method for incompressible non-Newtonian flows, J. Comp. Phys. 36 (1980) 313.
[8] E.J. O'Donovan, R.I. Tanner, Numerical study of the Bingham squeeze film problem, J. Non-Newtonian Fluid Mech. 15 (1984) 75.

[9] G.R. Burgos, A.N. Alexandrou, V. Entov, On the determination of yield surfaces in Herschel–Bulkley fluids, J. Rheol. 43 (1999) 463.
[10] K.R.J. Ellwood, G.C. Georgiou, T.C. Papanastasiou, J.O. Wilkes, Laminar jets of Bingham-plastic liquids, J. Rheol.gy 34 (1990) 787.
[11] E. Mitsoulis, S.S. Abdali, N.C. Markatos, Flow simulation of Herschel–Bulkley fluids through extrusion dies, Can. J. Chem. Eng. 71 (1993) 147.
[12] J.A. Tsamopoulos, M.F. Chen, A.V. Borkar, On the spin coating of viscoplastic fluids, Rheol. Acta 35 (1996) 597.
[13] J. Blackery, E. Mitsoulis, Creeping motion of a sphere in tubes filled with a Bingham plastic material, J. Non-Newtonian Fluid Mech. 70 (1997) 59.
[14] M. Beaulne, E. Mitsoulis, Creeping motion of a sphere in tubes filled with Herschel–Bulkley fluids, J. Non-Newtonian Fluid Mech. 72 (1997) 55.
[15] G.R. Burgos, A.N. Alexandrou, Flow development of Herschel–Bulkley fluids in a sudden 3-D square expansion, J. Rheol. 43 (1999) 485.
[16] D.N. Smyrnaios, J.A. Tsamopoulos, Squeeze flow of Bingham plastics, J. Non-Newtonian Fluid Mech. 100 (2001) 165.
[17] A.N. Alexandrou, T.M. McGilvreay, G. Burgos, Steady Herschel–Bulkley fluid flow in three-dimensional expansions, J. Non-Newtonian Fluid Mech. 100 (2001) 77.
[18] M. Keentok, J.F. Milthorpe, E. O'Donovan, On the shearing zone around rotating vanes in plastic liquids: theory and experiment, J. Non-Newtonian Fluid Mech. 17 (1985) 23.
[19] N.Q. Dzuy, D.V. Boger, Direct yield stress measurement with the vane method, J. Rheol. 29 (1985) 334.
[20] A.N. Alexandrou, E. Duc, V. Entov, Inertial, viscous and yield stress effects in Bingham fluid filling of a 2-D cavity, J. Non-Newtonian Fluid Mech. 96 (2001) 383.
[21] C.J. Paradies, M. Rappaz, in: B.G. Thomas, C. Beckermann (Eds.), Modeling the Rheology of Semisolid Metal Alloys During Die Casting, Modeling of Casting, Welding and Advanced Solidification Processes VIII, Proceedings of the 8th International Conference on Modeling of Casting and Welding Processes, San Diego, 7–12 June 1998, p. 933.
[22] J. Koke, M. Modigell, M. Hufschmidt, A.N. Alexandrou, A study on the die filling behavior with semisolid fluids, in: Proceedings of the 6th International Conference on Semisolid Processing of Alloys and Composites, Turin, 27–29 September 2000, p. 635.
[23] K. Housiadas, G. Georgiou, J. Tsamopoulos, The steady annular extrusion of a Newtonian liquid under gravity and surface tension, Int. J. Numer. Meth. Fluids 33 (2000) 1099.
[24] G. Georgiou, Annular liquid jets at high Reynolds numbers, Int. J. Numer. Methods Fluids 42 (2003) 117.